




First Observation of New Flat Line Fano Profile via an X-Ray Planar Cavity

Zi-Ru Ma (马子茹),¹ Xin-Chao Huang (黄新朝),^{1,*} Tian-Jun Li (李天钧)¹,
 Hong-Chang Wang (王洪昌),² Gen-Chang Liu (刘根长),³ Zhan-Shan Wang (王占山),³ Bo Li (李波),¹
 Wen-Bin Li (李文斌),^{3,†} and Lin-Fan Zhu (朱林繁)^{1,‡}

¹*Hefei National Research Center for Physical Sciences at Microscale and Department of Modern Physics, University of Science and Technology of China, Hefei, Anhui 230026, People's Republic of China*

²*Diamond Light Source, Harwell Science and Innovation Campus, Didcot, Oxfordshire, OX11 0DE, United Kingdom*

³*MOE Key Laboratory of Advanced Micro-Structured Materials, Institute of Precision Optical Engineering (IPOE), School of Physics science and Engineering, Tongji University, Shanghai 200092, People's Republic of China*

 (Received 16 September 2021; revised 10 November 2021; accepted 27 September 2022; published 16 November 2022)

A new Fano profile of a flat line is achieved experimentally by manipulating the relative amplitude of the continuum path, when q takes the pure imaginary number of $-i$ in the x-ray regime. The underlying mechanism is that the interference term in the scattering will cancel the discrete term exactly. This new Fano profile renders only an observable continuum along with an invisible response to the discrete state of atomic resonance. The results suggest not only a different strategy to invisibility studies which provides a possible tool to identify weaker structures hidden by the strong white line, but also a new scenario to enrich the manipulations of two-path interference and nonlinear Fano resonance.

DOI: [10.1103/PhysRevLett.129.213602](https://doi.org/10.1103/PhysRevLett.129.213602)

The Fano formula, describing the ubiquitous interference between a nonresonant continuum and a resonant discrete state, is one of the most important formulas in modern physics to depict the complex physical phenomena in nuclear physics, atomic, molecular and optical physics, condensed-matter physics, chemistry, etc. [1–7]. The key parameter in the Fano formula is the line profile index q , and in Fano's original treatment, q takes a real number. According to the values of q , the Fano profile can be divided into two types, i.e., symmetric and asymmetric line shapes. The former corresponds to the zero (window resonance) and infinite (Lorentzian-shaped resonance) values of q , while the latter takes other values. Further studies revealed that q can take a complex number in quantum systems with decoherence, such as quantum dots [8,9], atomic systems [6], cavities [10], and plasmonic systems [11]. It is realized that a complex q is a signature of dephasing and dissipation in systems and results from the breaking of time-reversal symmetry [12]. Subsequent theoretical studies on the complex q demonstrate that the imaginary part of q [$\text{Im}(q)$] makes the original Fano formula be superimposed by an additional Lorentzian function [12–16]. More surprisingly, theory predicts a new type of Fano line shape of a flat line induced by the effect of $\text{Im}(q)$ [14], which has never been verified experimentally due to the difficulties in manipulating $\text{Im}(q)$ over a wide range [12]. In this Letter, by engineering the relative amplitude of the two paths, the unobserved new type of Fano profile of a flat line is demonstrated experimentally with a thin film planar cavity.

We find that the new Fano profile creates an invisible illusion of the discrete state, and the interesting

phenomenon is similar to plasmon-based optical, mechanical and elastic cloaking [17–19]. In our system, the discrete state is the core-level intense dipole white line transition in the hard x-ray regime. It should be noted that due to the interference between the continuum and specific discrete paths, only the intensity of the white line transition is smeared out, and other atomic transition signals could still exist. Therefore, the elimination of the white line will make the nearby weak structures be effectively identified, such as quadrupolar (QR) transitions [20–26], which are of great significance in deriving the atomic orbital, spin magnetic moments, local electronic structure, symmetry, valence and atomic environment [27,28]. Mitigating the obstacle of the strong dipole transition to the weak QR transitions is a long-standing topic in core-level spectroscopies [20–23,29–32]. Therefore, the demonstration of the flat Fano profile by manipulating $\text{Im}(q)$ over a wide range in this Letter might provide extensive applications for x-ray core-level spectroscopies and extend the cloaking topic to the even hard x-ray regime.

Introducing the large space in $\text{Im}(q)$ in an experiment is a challenging task. The changing range for $\text{Im}(q)$ caused by the system dissipation is limited. Here is another possible way that the complex q space is regulated by the relative amplitude between the continuum and discrete states [12,33], which could enlarge the $\text{Im}(q)$ range with a fixed phase. Obviously, controlling the relative amplitude is inadequate in atomic autoionization excitations [1,2]. The thin film planar cavity, which is an outstanding system for manipulating the light-matter interaction in the x-ray regime, casts alternative light into the manipulatable

two-path interference in both phase and the relative amplitude. In the past ten years, novel fundamental phenomena [3,4,34–41], including Fano resonance, have been realized via x-ray planar cavities with nuclear ensemble systems [3] and atomic systems [4,39]. In particular, the investigations about the superradiance and the phase manipulation in Fano resonance indicate that the thin-film planar cavity provides a versatile platform for the research of q on a complex plane [42]. The phase of the cavity is controlled by the incident angle in previous studies [3,4,39], while amplitude control has not been demonstrated. In this Letter, the phase is fixed to $\pi/2$ with $\text{Re}(q)$ taking zero, and a wide range regulation of $\text{Im}(q)$ is achieved by controlling the relative amplitude.

Figure 1(a) depicts the cavity structure, which is made of a multilayer of Pt and C with nanometers thickness. The layers of Pt are used as mirrors, and the layers of C are used to stack the cavity space. At a certain incident angle, x ray excites a specific cavity mode with a broad spectral width of approximately few hundreds eV, so it can serve as an “artificial” continuum state. An ultrathin WSi_2 layer is employed inside the cavity, and the remarkable white line around the L_{III} edge of W at $E_0 = 10208$ eV with $\gamma_0 = 7.2$ eV serves a resonant channel relating to an electric dipole allowed transition from the inner shell $2p$ to the unoccupied $5d$ energy level [43]. The atomic layer couples with the cavity mode, and both the scattering amplitudes r_c and r_a from the bare cavity itself and the atomic resonance are detected in the reflection direction, i.e., forming a Fano-type two-path interference [3,4,39]. As shown in the right top of Fig. 1(b), the asymmetrical Fano line shape can be easily manipulated by changing the q factor by modifying the relative phase of the two paths controlled by the angle offset [3,4,39]. At $\theta = \theta_c$, where the relative phase is fixed to $\pi/2$, the real part of q is 0, and the Fano profile evolution can be studied by controlling $\text{Im}(q)$, which leads to the emergence of the flat line, i.e., the new type of Fano profile depicted at the bottom of Fig. 1(b).

The description of the interferometer has been well established by the quantum model [4,51], and the resonant scattering r_a of the atom and the scattering r_c of the cavity itself are given in the reflection direction. After fixing the phase at the mode angle, the two-path interference is given in Eq. (1) as

$$r_a = -c' \frac{\gamma_c}{\Gamma} \frac{i\Gamma}{\Delta + i\Gamma}, \quad r_c = -1 + c', \quad r = r_a + r_c. \quad (1)$$

Note here that Eq. (1) is derived from the general Fano interference (Supplemental Material, Sec. II [44]) with a fixed phase of $\pi/2$. $\Gamma = \gamma_c + \gamma_0$, where γ_0 is the natural decay rate of the atom, and γ_c is the enhanced emission rate arising from the cavity effect and superradiance. The energy detuning $\Delta = E - E_0$. $c' = (2\kappa_R/\kappa)$, where κ is the decay rate of the cavity and κ_R is the coupling strength of the external classical x-ray field into the cavity mode,

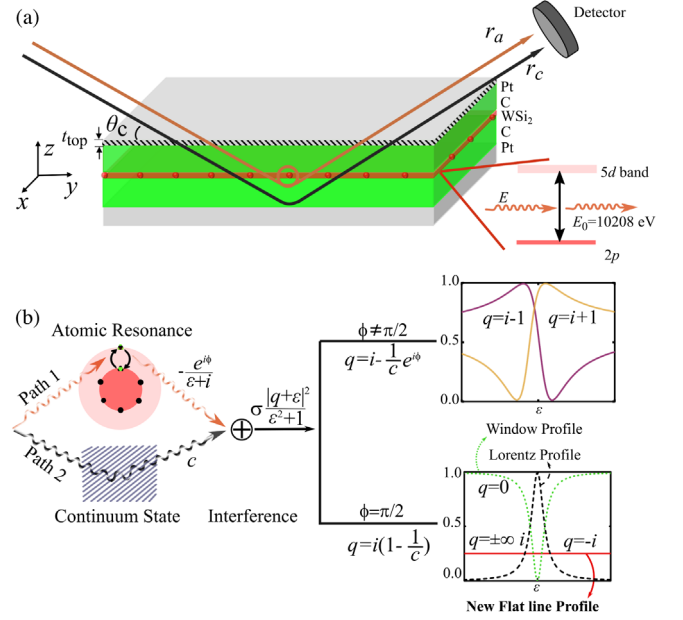


FIG. 1. (a) The two-path interferometer is built by an x-ray planar cavity with an embedded ultrathin atomic layer. In the present Letter, three cavity samples with different t_{top} values of 0, 1.0, and 2.2 nm are prepared [44]. The inset shows the energy levels of atom W, E is the incident x-ray energy and $E_0 = 10208$ eV is the transition energy of the W atom. (b) Conception of the two-path interference mechanism. ϕ is the relative phase of the two paths. If $\phi \neq \pi/2$, q is a complex number. The Fano interference spectra are the asymmetrical lines, as shown at the top. The orange and purple lines correspond to positive and negative $\text{Re}(q)$, respectively. If $\phi = \pi/2$, the parameter q is a pure imaginary number, and generally symmetric Lorentz line or window resonance is observed. However, when $\text{Im}(q)^2 = 1$, the spectrum becomes a flat line (the red solid line in the right inset), which is equal to the intensity of the continuum path.

and they are real numbers when the phase is fixed at $\pi/2$. As we will show below that c' is the key factor in the present study, whose value can be experimentally adjusted by changing the thickness of the top Pt layer t_{top} , resulting in a manipulatable pure imaginary q . To clearly show the manipulability of the two-path interferometer, the amplitude r of reflectivity can be simplified as a universal form $c - [i/(\varepsilon + i)]$. As depicted in Fig. 1(b), c is the relative amplitude of the ideal continuum state, and $a = [-i/(\varepsilon + i)]$ is from an ideal Lorentzian resonance with $\varepsilon = [\Delta/(\Gamma/2)]$. Evidently, we can write $|r|^2$ as a Fano profile,

$$R = \sigma \frac{|q + \varepsilon|^2}{\varepsilon^2 + 1}, \quad q = i \left(1 - \frac{1}{c}\right), \quad (2)$$

$$\sigma = \left| c' \frac{\gamma_c}{\Gamma} \right|^2 c^2, \quad c = \frac{c' - 1}{c'} \frac{\Gamma}{\gamma_c},$$

where $R = |r|^2$ is the reflection intensity. It can be seen clearly that the asymmetry parameter q is a pure imaginary

and is directly determined by the relative amplitude c (Supplemental Material, Sec. II [44]), which means that the profiles are always symmetric. $\text{Im}(q)$ can be directly controlled by the manipulatable experimental factor c' because Γ/γ_c varies slowly. When $\text{Im}(q)$ is tailored as we wish, the Fano profile of R will be strongly modified,

$$R = \sigma \left(\frac{\varepsilon^2}{\varepsilon^2 + 1} + \frac{\text{Im}(q)^2}{\varepsilon^2 + 1} \right). \quad (3)$$

The complex q produces the equivalent of superimposing a Lorentz formula with amplitude $\text{Im}(q)^2$ on the original Fano form. As depicted by the two-path schematic in Fig. 1(b), when $\text{Im}(q)$ takes the value of 0, R is the well-known window resonance with a symmetric spectral dip. With increasing $|\text{Im}(q)|$, the amplitude of the additional Lorentz becomes larger, and the window profile becomes shallower and shallower and even inverted. When $|\text{Im}(q)| > 1$, the parameter $\text{Im}(q)$ reverses the profile of window resonance, which means that the window resonance and the Lorentz resonance can be mutually transformed by engineering $\text{Im}(q)$. The most attractive situation is that when $\text{Im}(q)^2$ takes a magic value of 1, R becomes a flat line, which is a new type of Fano profile, and the reflection intensity is equal to c^2 that is just from the ideal continuum path. This particular case creates an illusion that the detector did not detect any response from the Lorentzian resonance path even though the transition does happen. The three representative situations can be concluded in Eq. (4) and depicted in Fig. 1(b),

$$R/\sigma' = \begin{cases} \frac{\varepsilon^2}{1+\varepsilon^2}, & \text{Im}(q) = 0, \text{ Window profile} \\ c^2, & \text{Im}(q) = -1, \text{ Constant} \\ \frac{1}{1+\varepsilon^2}, & \text{Im}(q) = \pm\infty, \text{ Lorentz profile.} \end{cases} \quad (4)$$

It should be noted that the reflectivity intensity can also be expressed as $R = \sigma' \{c^2 + [(-2c)/(\varepsilon^2 + 1)] + [1/(\varepsilon^2 + 1)]\}$ [44], where c^2 and $[1/(\varepsilon^2 + 1)]$ are the intensities from the contributions of the ideal continuum path and Lorentzian discrete path separately, and $[(-2c)/(\varepsilon^2 + 1)]$ represents the interference conjugate item. When the value of $\text{Im}(q)$ is -1 , i.e., $c = \frac{1}{2}$, the conjugate item $[(-2c)/\varepsilon^2 + 1]$ will exactly cancel out $[1/(\varepsilon^2 + 1)]$, that is, the discrete state of atomic resonance is invisible, which could provide a novel strategy to the modern invisibility cloaking topic [17,18] and suggest a new method to eliminate the influence of the intense white line on the weak peaks. Note here again that the relative phase between the discrete and continuum states is fixed for the present scenario, which is different from previous studies [3,4,39].

To more clearly show the key role of $\text{Im}(q)$, the numerical results of Eq. (4) are shown in Figs. 2(a) and 2(b), where with $\text{Im}(q)^2$ increasing the transformation from

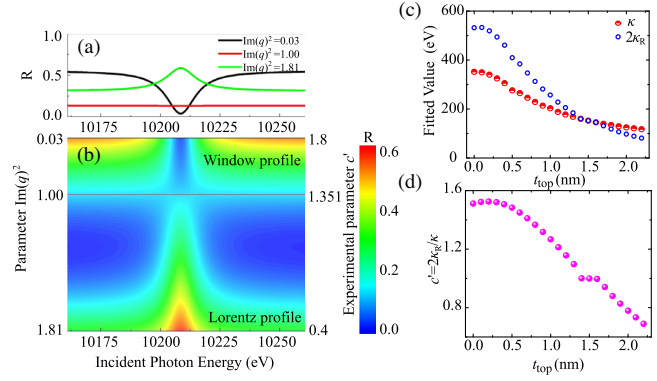


FIG. 2. (a) Numerical reflectivity as a function of energy at different amplitudes of c' . (b) A numerical 2D map of the reflection spectrum vs the energy and $\text{Im}(q)^2$ (c'). The reflectivity becomes a constant when $\text{Im}(q)^2 = 1$ ($c' = 1.351$). Herein, $\gamma_0 = 7.2$, $\gamma_c = 7.6$, and $E_0 = 10208$ eV are used from the sample of $t_{\text{top}} = 1.0$ nm (Supplemental Material, Table S2 [44]). (c) and (d) The cavity properties of Pt (t_{top})/C (19.8 nm)/WSi₂ (2 nm)/C (20.2 nm)/Pt (15.0 nm)/Si (substrate) simulated by the Parratt formalism with t_{top} varying from 0.0 to 2.2 nm (more details are shown in Fig. S5 and Supplemental Material, Sec. III [44]). (c) The fitted κ and κ_R as a function of t_{top} and (d) the c' derived from (c).

the window profile to the Lorentz profile, including the flat line, is clearly depicted. To experimentally observe this interesting phenomenon of a new type of Fano profile, the most difficult challenge is to design c' with remarkable variations since $\text{Im}(q)$ is directly connected with c' . As mentioned before, $c' = (2\kappa_R/\kappa)$, where κ_R depends on the thickness of the top mirror layer t_{top} , i.e., the thinner the top mirror layer is, the easier the x-ray coupling into the cavity mode, so the larger the value of κ_R . κ is also related to t_{top} , but it varies more slowly compared to κ_R , as shown in Fig. 2(c). Therefore, the factor c' monotonically decreases, as shown in Fig. 2(d). This suggests that although κ_R and κ cannot be adjusted separately, the key parameter of c' can be controlled directly by changing the thickness of the top mirror layer, i.e., $\text{Im}(q)^2$ can be adjusted well. The thickness manipulation of the top mirror layer was very recently suggested to perform the inverse design of artificial two-level systems by Diekmann *et al.*, which was brought to our attention [52].

The measurement was performed at the B16 test beam line of the Diamond Light source, which has a double-crystal monochromator (Si-111) with an energy resolution of approximately 1.0 eV at 10 keV. To experimentally control the relative scattering amplitude of the continuum in the x-ray planar cavity system, three cavities were delicately designed and prepared with different values of t_{top} of 0, 1.0, and 2.2 nm to ensure remarkable variations for factor c' , and cross-sectional transmission electron microscopy (TEM), atomic force microscopy (AFM), and energy dispersive x-ray spectroscopy (EDX) were carried out to

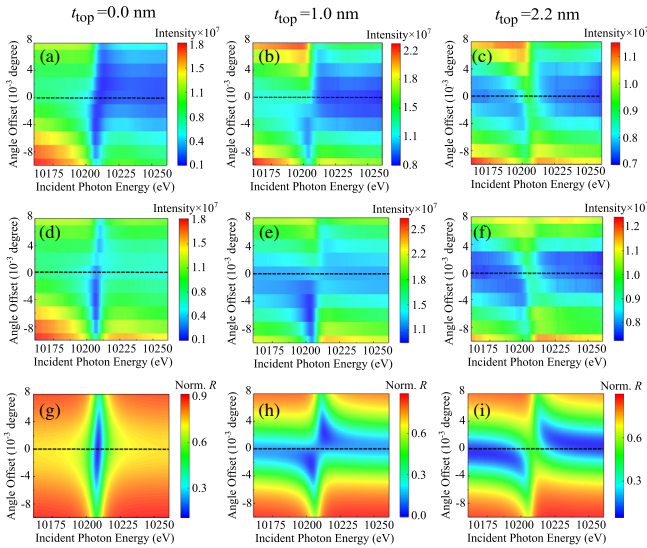


FIG. 3. The 2D maps of the reflectivity spectra vs the energy and angle offset. (a)–(c) Reflectivity spectra of the samples with t_{top} values of 0, 1.0, and 2.2 nm. The zero angle offsets of the y-axis are located at 0.222° , 0.216° , and 0.216° . Panels (d)–(f) show the experimental results of (a)–(c), with the absorption edge being subtracted. Panels (g)–(i) show the calculations by the quantum optics model with the experimental parameters in Table S2 [44] used. From the left to the right panels, the conversion from valleys to peaks is clearly observed at the corresponding mode angles (dashed lines).

confirm the compositions and structures of the cavity [44] (Supplemental Material, Sec. I). The off-resonance $\theta - 2\theta$ rocking curves were first measured to find the first order of the cavity mode and were fitted to determine the multilayer structures for the three cavities (Supplemental Material, Fig. S1, Table S1 [44]). In the measurement for each cavity sample, the angle offset was slightly changed around the first cavity mode, and the incident photon energy E was scanned from 10 161 to 10 261 eV across the resonant energy E_0 to record the reflectivity spectra.

The experimental reflectivity spectra for the three cavity samples as a function of the incident x-ray energy E and angle offset are shown in Figs. 3(a)–3(c). It should be noted that some complexities arise under nonideal experimental conditions. For instance, we can see that the nonbalanced intensities in the high-energy and low-energy sides of the resonance appear in the reflectivity spectra at all angles because the absorption edge overlaps with the white line at higher energy. The absorption edge is very difficult to be considered in the quantum model, while it is easy to be removed in mathematics. To remove the influence of the absorption edge, the experimental reflectivity spectra were fitted by combining the quantum formula with a Heaviside step function $H(E)$, which is used to consider the steplike contribution of the absorption edge [44] (Supplemental Material, Sec. IV). Then, the clean Fano profile evolution is extracted as shown in Figs. 3(d)–3(f). Now, the dispersion

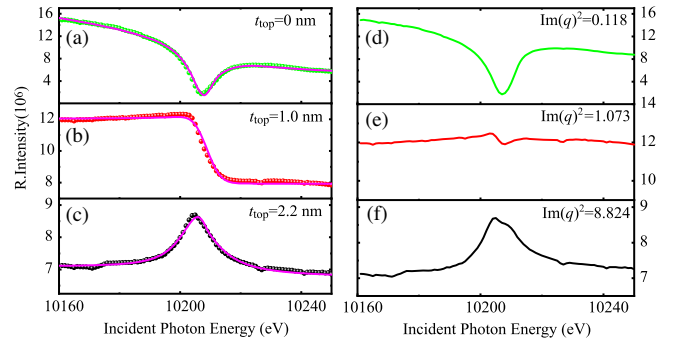


FIG. 4. (a)–(c) The experimental and fitted reflectivity spectra at model angles of the three samples with different t_{top} as a function of incident photon energy. The dots are the experimental results, and the pink solid lines are the fitted results. (d)–(f) The extracted results after discarding the contributions of the absorption edge.

relation and the intensities in the high energy and low energy sides far from the resonance are almost the same. Figures 3(g)–3(i) show the reflectivities of the resonance response according to the quantum model. The quantum model simplifies the analysis of complex physical processes without taking the inhomogeneities of the sample, the experimental measurement instability, etc. Even so, the features of the measured data in Figs. 3(d)–3(f) are identified with the quantum model theory very well. We can see from Figs. 3(d)–3(f) that the interference of the two paths of the reflectances of cavity and atomic resonant scattering leads to the typical Fano profile evolution from asymmetric to symmetric and back to asymmetric, with asymmetry controlled by the angle offset (i.e., the phase between the paths of the continuum and discrete). This can be well predicted by the quantum optics model and is observed in all three cavity samples [44] (Supplemental Material, Sec. II). Because the phase depends on the cavity detuning Δ_c , i.e., the angle offset, the phase is fixed to $\pi/2$ when θ is very close to the mode angle θ_c (angle offset is zero, as labeled by the dashed lines in Fig. 3), which corresponds to the zero value of $\text{Re}(q)$ and the symmetric line shapes (Supplemental Material, Sec. II [44]). In this case, by changing the pure imaginary number $\text{Im}(q)$, the Fano profile conversion from a symmetric peak to a symmetric window dip can be revealed, and the observation is achieved by changing the thickness of the top layer Pt, as shown at the corresponding mode angles in Figs. 3(d)–3(f). Moreover, we can see a nearly perfect flat line at the mode angle in Figs. 3(e) and 3(h), as predicted by the theory above.

To more clearly exhibit the conversion between the symmetric dip and symmetric peak, the reflectivity spectra along with the absorption edge subtracted ones at the mode angles are shown in Figs. 4(a)–4(c) and 4(d)–4(f), respectively. Figures 4(a)–4(c) show that the fitted results agree well with the experimental results, and only an edge is

observed in Fig. 4(b) without a resonant profile. After subtracting the absorption edge, the same behavior as discussed in Figs. 2(a)–2(b) is exhibited in Figs. 4(d)–4(f). When $\text{Im}(q)^2$ increases from 0.118 of $t_{\text{top}} = 0.0$ nm [Fig. 4(d)] to 8.824 of $t_{\text{top}} = 2.2$ nm [Fig. 4(f)], the reflectivity spectra change from a spectral dip (window profile) to a spectral peak (Lorentz profile). The new Fano profile of the flat line is realized when $t_{\text{top}} = 1.0$ nm [Fig. 4(e)] at $\text{Im}(q) = -1.036$ with $\text{Im}(q)^2 = 1.073$, which is extremely close to the ideal flat line case of $\text{Im}(q) = -1$, and the reflection spectrum only shows a very tiny peak. On the other hand, the window and Lorentz profiles show slight asymmetry, which is caused by a tiny angle deviation from the cavity mode in the experiment due to the accuracy and stability of the goniometer [3,4].

In conclusion, the new type of Fano profile of the flat line is realized experimentally for the first time based on the pure imaginary q modulation. The Fano interferometer used here is built by an x-ray planar cavity, in which the amplitude regulation of the continuum path enlarges the $\text{Im}(q)$ space. With the large range of $\text{Im}(q)$, the window-Lorentz profile conversion is observed experimentally, and the new Fano profile of the flat line emerges when the value of $\text{Im}(q)$ approaches -1 . The new Fano profile has an interesting behavior in which the interference term cancels the discrete path exactly, and it creates an invisible illusion of the discrete state, which could open a novel strategy to the object invisibility topic [17,19], even in the hard x-ray regime. The invisible illusion can identify weaker structures near the intense white line in the x-ray spectrum, which may merge the cloaking topic with x-ray core-level spectroscopies. Furthermore, enlarging the complex q space based on amplitude regulation would bring new opportunities for decoherence studies [12]. Multipaths interference is a common effect in extensive quantum systems, e.g., waveguide-transmon qubits [53], coupled microcavity resonators [54], metamaterials [55], etc., and this Letter could contribute to a better understanding of the complex spectra of such quantum devices.

We thank Zhen-Sheng Yuan for useful discussions. This work is supported by the National Natural Science Foundation of China (Grant No. U1932207) and the National Key Research and Development Program of China (Grants No. 2017YFA0303500 and No. 2017YFA0402300). The experiment was carried out with a beam time approved by Diamond Light Source Ltd. (No. MM21446-1 on instrument B16), United Kingdom.

*xinchao.huang@xfel.eu

†wbli@tongji.edu.cn

‡lfzhu@ustc.edu.cn

[1] U. Fano, *Phys. Rev.* **124**, 1866 (1961).

[2] U. Fano and J. W. Cooper, *Phys. Rev.* **137**, A1364 (1965).

- [3] K. P. Heeg, C. Ott, D. Schumacher, H.-C. Wille, R. Röhlberger, T. Pfeifer, and J. Evers, *Phys. Rev. Lett.* **114**, 207401 (2015).
- [4] J. Haber, J. Gollwitzer, S. Francoual, M. Tolkiehn, J. Strempler, and R. Röhlberger, *Phys. Rev. Lett.* **122**, 123608 (2019).
- [5] C. Ott, A. Kaldun, P. Raith, K. Meyer, M. Laux, J. Evers, C. H. Keitel, C. H. Greene, and T. Pfeifer, *Science* **340**, 716 (2013).
- [6] A. Zielinski, V. P. Majety, S. Nagele, R. Pazourek, J. Burgdörfer, and A. Scrinzi, *Phys. Rev. Lett.* **115**, 243001 (2015).
- [7] A. E. Miroshnichenko, S. Flach, and Y. S. Kivshar, *Rev. Mod. Phys.* **82**, 2257 (2010).
- [8] K. Kobayashi, H. Aikawa, S. Katsumoto, and Y. Iye, *Phys. Rev. Lett.* **88**, 256806 (2002).
- [9] K. Kobayashi, H. Aikawa, S. Katsumoto, and Y. Iye, *Phys. Rev. B* **68**, 235304 (2003).
- [10] S. Rotter, U. Kuhl, F. Libisch, J. Burgdörfer, and H.-J. Stöckmann, *Physica (Amsterdam)* **29E**, 325 (2005).
- [11] B. Gallinet and O. J. F. Martin, *Phys. Rev. B* **83**, 235427 (2011).
- [12] A. Bärnthaler, S. Rotter, F. Libisch, J. Burgdörfer, S. Gehler, U. Kuhl, and H.-J. Stöckmann, *Phys. Rev. Lett.* **105**, 056801 (2010).
- [13] D. Finkelstein-Shapiro, I. Urdaneta, M. Calatayud, O. Atabek, V. Mujica, and A. Keller, *Phys. Rev. Lett.* **115**, 113006 (2015).
- [14] I. Avrutsky, R. Gibson, J. Sears, G. Khitrova, H. M. Gibbs, and J. Hendrickson, *Phys. Rev. B* **87**, 125118 (2013).
- [15] D. Finkelstein-Shapiro and A. Keller, *Phys. Rev. A* **97**, 023411 (2018).
- [16] D. Finkelstein-Shapiro, M. Calatayud, O. Atabek, V. Mujica, and A. Keller, *Phys. Rev. A* **93**, 063414 (2016).
- [17] P. Chen, J. Soric, and A. Alù, *Adv. Mater.* **24**, OP281 (2012).
- [18] X. Xu, C. Wang, W. Shou, Z. Du, Y. Chen, B. Li, W. Matusik, N. Hussein, and G. Huang, *Phys. Rev. Lett.* **124**, 114301 (2020).
- [19] M. V. Rybin, D. S. Filonov, P. A. Belov, Y. S. Kivshar, and M. F. Limonov, *Sci. Rep.* **5**, 8774 (2015).
- [20] J. C. Lang, G. Srajer, C. Detlefs, A. I. Goldman, H. König, X. Wang, B. N. Harmon, and R. W. McCallum, *Phys. Rev. Lett.* **74**, 4935 (1995).
- [21] M. H. Krisch, C. C. Kao, F. Sette, W. A. Caliebe, K. Hämäläinen, and J. B. Hastings, *Phys. Rev. Lett.* **74**, 4931 (1995).
- [22] F. Bartolomé, J. M. Tonnerre, L. Seve, D. Raoux, J. Chaboy, L. M. Garcia, M. Krisch, and C. C. Kao, *Phys. Rev. Lett.* **79**, 3775 (1997).
- [23] J. Danger, P. Le Fèvre, H. Magnan, D. Chandesris, S. Bourgeois, J. Jupille, T. Eickhoff, and W. Drube, *Phys. Rev. Lett.* **88**, 243001 (2002).
- [24] N. M. Souza-Neto, D. Haskel, Y.-C. Tseng, and G. Lapertot, *Phys. Rev. Lett.* **102**, 057206 (2009).
- [25] Y. Liang, J. Vinson, S. Pemmaraju, W. S. Drisdell, E. L. Shirley, and D. Prendergast, *Phys. Rev. Lett.* **118**, 096402 (2017).
- [26] T. C. Rossi, D. Grolimund, M. Nachttegaal, O. Cannelli, G. F. Mancini, C. Bacellar, D. Kinschel, J. R. Rouxel,

- N. Ohannessian, D. Pergolesi *et al.*, *Phys. Rev. B* **100**, 245207 (2019).
- [27] F. De Groot, *Chem. Rev.* **101**, 1779 (2001).
- [28] M. Rovezzi and P. Glatzel, *Semicond. Sci. Technol.* **29**, 023002 (2014).
- [29] K. Hämäläinen, D. P. Siddons, J. B. Hastings, and L. E. Berman, *Phys. Rev. Lett.* **67**, 2850 (1991).
- [30] L. Journel, J.-M. Mariot, J.-P. Rueff, C. F. Hague, G. Krill, M. Nakazawa, A. Kotani, A. Rogalev, F. Wilhelm, J.-P. Kappler, and G. Schmerber, *Phys. Rev. B* **66**, 045106 (2002).
- [31] R. F. Pettifer, S. P. Collins, and D. Laundry, *Nature (London)* **454**, 196 (2008).
- [32] R. Dos Reis, L. Veiga, C. Escanhoela Jr, J. Lang, Y. Joly, F. Gandra, D. Haskel, and N. Souza-Neto, *Nat. Commun.* **8**, 1203 (2017).
- [33] A. A. Clerk, X. Waintal, and P. W. Brouwer, *Phys. Rev. Lett.* **86**, 4636 (2001).
- [34] R. Röhlberger, K. Schlage, B. Sahoo, S. Couet, and R. Rüffer, *Science* **328**, 1248 (2010).
- [35] R. Röhlberger, H. Wille, K. Schlage, and B. Sahoo, *Nature (London)* **482**, 199 (2012).
- [36] K. P. Heeg, H.-C. Wille, K. Schlage, T. Guryeva, D. Schumacher, I. Uschmann, K. S. Schulze, B. Marx, T. Kämpfer, G. G. Paulus, R. Röhlberger, and J. Evers, *Phys. Rev. Lett.* **111**, 073601 (2013).
- [37] K. P. Heeg, J. Haber, D. Schumacher, L. Bocklage, H.-C. Wille, K. S. Schulze, R. Loetzsch, I. Uschmann, G. G. Paulus, R. Rüffer, R. Röhlberger, and J. Evers, *Phys. Rev. Lett.* **114**, 203601 (2015).
- [38] J. Haber, X. Kong, C. Strohm, S. Willing, J. Gollwitzer, L. Bocklage, R. Rüffer, A. Pálffy, and R. Röhlberger, *Nat. Photonics* **11**, 720 (2017).
- [39] X.-C. Huang, X.-J. Kong, T.-J. Li, Z.-R. Ma, H.-C. Wang, G.-C. Liu, Z.-S. Wang, W.-B. Li, and L.-F. Zhu, *Phys. Rev. Res.* **3**, 033063 (2021).
- [40] B. W. Adams, C. Buth, S. M. Cavaletto, J. Evers, Z. Harman, C. H. Keitel, A. Pálffy, A. Picón, R. Röhlberger, Y. Rostovtsev *et al.*, *J. Mod. Opt.* **60**, 2 (2013).
- [41] R. Röhlberger and J. Evers, *Mod. Mössbauer Spectrosc.* **137**, 105 (2021).10.1007/978-981-15-9422-9_3
- [42] T. J. Li, X. C. Huang, Z. R. Ma, B. Li, and L. F. Zhu, *Phys. Rev. Res.* **4**, 023081 (2022).
- [43] M. Brown, R. E. Peierls, and E. A. Stern, *Phys. Rev. B* **15**, 738 (1977).
- [44] See Supplemental Material at <http://link.aps.org/supplemental/10.1103/PhysRevLett.129.213602> for details on theoretical model and additional results, which includes Refs. [45–50].
- [45] M. Björck and G. Andersson, *J. Appl. Crystallogr.* **40**, 1174 (2007).
- [46] X. C. Huang, W. B. Li, X. J. Kong, and L. F. Zhu, *Opt. Express* **25**, 31337 (2017).
- [47] M. Tomaš, *Phys. Rev. A* **51**, 2545 (1995).
- [48] R. Röhlberger, K. Schlage, T. Klein, and O. Leupold, *Phys. Rev. Lett.* **95**, 097601 (2005).
- [49] K. P. Heeg and J. Evers, *Phys. Rev. A* **91**, 063803 (2015).
- [50] L. G. Parratt, *Phys. Rev.* **95**, 359 (1954).
- [51] K. P. Heeg and J. Evers, *Phys. Rev. A* **88**, 043828 (2013).
- [52] O. Diekmann, D. Lentrodt, and J. Evers, *Phys. Rev. A* **105**, 013715 (2022).
- [53] M. Mirhosseini, E. Kim, X. Zhang, A. Sipahigil, P. B. Dieterle, A. J. Keller, A. Asenjo-Garcia, D. E. Chang, and O. Painter, *Nature (London)* **569**, 692 (2019).
- [54] M. F. Yanik, W. Suh, Z. Wang, and S. Fan, *Phys. Rev. Lett.* **93**, 233903 (2004).
- [55] Y. Hu, W. Liu, Y. Sun, X. Shi, J. Jiang, Y. Yang, S. Zhu, J. Evers, and H. Chen, *Phys. Rev. A* **92**, 053824 (2015).